Electromagnetic tomography measuring bench for estimating the density of materials

Cyrille Fauchard, Imen Boughanmi, Nabil Benjelloun, Riah Zouheir, Théau Cousin, Bruno Beaucamp, Vincent Guilbert

NDT&E International 147 (2024) 103212

Contents lists available at ScienceDirect

NDT and E International

journal homepage: www.elsevier.com/locate/ndteint

Research Paper

Electromagnetic tomography measuring bench for estimating the density of materials

Cyrille Fauchard [a,*], Imen Boughanmi [a,b], Nabil Benjelloun [b], Riah Zouheir [b], Théau Cousin [c,d], Bruno Beaucamp [a], Vincent Guilbert [a]

[a] Cerema, Research Team ENDSUM, 10 chemin de la poudriére, Le Grand-Quevilly, 76120, France
[b] ESIGELEC, IRSEEM, UNIROUEN, Rouen, 76000, France
[c] INSA de Rouen, LMI (EA 3226 - FR CNRS 3335), 685 Avenue de l'Université, Saint-Étienne-du-Rouvray, 76801, France
[d] Routes de France, 9, rue de Berri, Paris, 75008, France

ARTICLE INFO

Keywords:
Electromagnetic tomography
Hot mix asphalt
Permittivity
Density

ABSTRACT

In the laboratory, the density of pavement cores (cylindrical samples of hot mix asphalt (HMA) material taken from roads) is assessed using an electromagnetic (EM) bench consisting of two ultra-wideband (UWB) Vivaldi antennas and a vector network analyser (VNA). The main objective is to replace the nuclear gauge system currently used in the laboratory as the standard method for this purpose. Firstly, specific antipodal Vivaldi antennas have been adapted from the literature. Their dimensions are 7 × 7 cm with a bandwidth [1.5–15 GHz]. Secondly, a tomographic approach is compared with an analytical solution and a Finite-Difference Time Domain (FDTD) simulation, based on a time-domain estimation of the dielectric under test (DUT) with a single transmitter/receiver configuration. A laboratory validation is presented and the adapted antennas as well as the time domain approach show acceptable results for assessing the dielectric constant on known materials. Finally, to show that the proposed EM bench is a promising non-ionizing solution, the density or equivalent compactness of HMA cylindrical samples is estimated and compared with nuclear gauge results.

1. Introduction

In the field of civil engineering, and more particularly in the road building, it is mandatory to control some physical parameters of the implemented materials with standard methods. These controls ensure that technical specifications have been followed, which are required to reach dimensions and mechanical characteristics that guarantee the best safety/cost ratio as well as an optimal lifetime. Among these parameters, density (or compactness) of bituminous materials (HMA) must be controlled since it is related to mechanical strength able to support traffic solicitations. Density is directly related to HMA air content and can be assessed on site or in the laboratory. HMA materials of newly-paved road are basically composed of rock aggregates, bituminous binder, filler (limestone powder) and air.

For on site control, nuclear methods based on back-scattered or transmitted gamma rays [1–4] exist but have become more and more rare since regulation is now very restrictive as far as concerned the use of nuclear sources (transport, maintenance, storage and exposure to ionizing radiations for users). Three kinds of alternatives EM solutions have been proposed in the last decade. First, it is now common to assess the on site density/compactness with low frequency EM methods [5]. Nevertheless, these on site EM methods still have to convince [6–8]. Al-Qadi et al. [9] followed by Leng et al. [10] used a Ground Penetrating Radar (GPR) system (i) to measure the dielectric constant of surface HMA layers and (ii) to assess the density based on mixing rules models given by Sihvola [11]. These models give the density in function of the measured dielectric constant of the mix and of the dielectric constant, the specific gravity and the mass content of each element compounding the mix. Nevertheless, the use of GPR for density/air void assessment remains questionable if users intend to assess this parameter with an error less than 2% of the true value, as shown in recent experiments performed by Prowell and Dudley [6]. Moreover, the drift of the GPR signal amplitude observed on many commercial GPR remains a problem [12]. Alternative and more stable solutions with a step frequency radar (SFR) using an ultra wide band (UWB) antenna and a VNA have demonstrated the ability to assess the density on site and in the laboratory on slabs samples [12–14], without EM signal drift encountered with GPR method, and including the increasingly frequent case of unknown recycle aggregates in HMA [15].

In the laboratory, density control can be performed by means of hydrostatic weighing. A mean value of the whole tested core is then

* Corresponding author.
E-mail address: cyrille.fauchard@cerema.fr (C. Fauchard).

https://doi.org/10.1016/j.ndteint.2024.103212
Received 17 October 2023; Received in revised form 21 July 2024; Accepted 7 August 2024
Available online 12 August 2024

obtain. The nuclear gauge in the laboratory (gamma bench) enable the density assessment in function of core height. This nuclear method is based on the emission of gamma rays by a nuclear source such as Cesium 137 and the reception after crossing the core by a device similar to a Geiger–Müller counter [16]. This method is standard and offer an accuracy less than 2% from the true density. Replacement of gamma bench is now a major issue since this method generates increasingly costs and constraints.

The objective of this work is to propose a non-nuclear solution to control the HMA density in the laboratory with an accuracy equivalent to the gamma bench. The proposed approach is an EM tomography system composed of two UWB antennas and a VNA, allowing the wave propagation through cylindrical samples to measure the dielectric constant of HMA, and then, to assess the density with mix models.

EM tomography is widely used in medical domain [17–21]. It allows the characterization of physical properties inside the human body to detect, for example, cancerous tumours [22]. Tomography can spatially reconstruct the complex dielectric properties of the studied medium from a few hundred MHz to a few GHz. EM tomography systems generally use an array containing several antennas [20,23–25]. The number of signals collected depends on the number of emitter/receivers pairs. This design requires that the antennas be small enough to be housed in a limited space, while maintaining a weak coupling between them. In addition, a necessary switching matrix device and several cables make the system complex and rather costly. Consequently, to avoid antenna couplings and complex operation of switching channels as well as to reduce the cost, a system with two mobile antennas is proposed in this work. This type of systems has already shown its capacity to reconstruct the dielectric properties of objects [26–30].

Several antennas have been proposed for different tomographic systems studied in the literature such as horn antennas [26,31], monopole antennas [32–35], bow-tie antennas [36,37] and Vivaldi antennas [25,38,39]. However, one of the structure that stands out among others in microwave imaging is the balanced antipodal Vivaldi antenna due to its UWB, gain and directivity properties [40,41].

Microwave imaging can be formulated in the frequency domain as well as in the time domain. In the frequency domain, single frequency measurements performed with a VNA are generally used to reconstruct the target profile, which simplifies the calculations but turns out to be inadequate for reconstructing very heterogeneous objects [27,28]. Several multi-frequency solutions have been introduced to improve the quality of imaging and the stability of the inversion algorithms [25,42,43]. Alternative approach consist to generate an EM pulse in the time domain, leading to a rapid acquisition. Such systems have been proposed for clinical applications [44–46]. We noticed that [47] performed permittivity measurement from [7 to 17 GHz], with an amplitude-phase analysis regression and by studying the waves passing trough cylindrical samples from the top to the bottom bases. The solution proposed here is based on a simple time domain analysis of EM-waves passing through cylindrical sample, perpendicular to its axis. This time domain analysis results from an Inverse Fourier Transform of the EM-waves from 1.5 GHz to 15 GHz generated by a VNA. Software developed in C language is used to control the analyser and move an emitter-receiver pair of ETSA along the axis of cylindrical cores from the top to the bottom bases.

In a first section, the theoretical basics of EM wave propagation through dielectric cylindrical sample is reminded and the simple tomography approach in time domain is explained, as well as FDTD simulation that helps to compare our results with measurements. This section also contains some signal processing to offer a good time resolution. In a second section, experiments are performed in the laboratory on cores and leads to permittivity assessment of the compactness/density of HMA samples. In the last section, a discussion proposes future developments to be considered to make the solution evolve towards a system allowing more complex acquisitions and a finer description of the dielectric properties of materials.

2. Theoretical backgrounds

2.1. Classical analytical model

The EM bench simulation is based on a TE^z polarization scattered by a circular cylinder considered as infitine in z direction, as shown in Fig. 1. The incident magnetic field can be written as [48]:

$$\mathbf{H}^i = H_0 e^{j\beta_0 x}\mathbf{e}_z = H_0 e^{j\beta_0\rho\ \cos(\phi)}\mathbf{e}_z = H_0 \sum_{n=-\infty}^{+\infty} j^{-n} J_n(\beta_0\rho) e^{jn\phi}\mathbf{e}_z \tag{1}$$

using Bessel functions properties and the Jacobi-Anger expansion. $\mathbf{e}_z$ is the unite vector, j the complex number satisfying $j^2 = -1$, (ρ, ϕ) the cylindrical coordinates, $\beta_0 = \frac{\omega}{c}$ the propagation factor, and $c = \frac{1}{\sqrt{\varepsilon_0\mu_0}} = 3.10^8$ ms^{-1} the speed of light in vacuum for ε_0 (resp. μ_0) the permittivity (resp. permeability) in free-space, defined as:

$$\begin{aligned} \varepsilon_0 &= 8.854187816\ 10^{-12}\ \text{F m}^{-1} \\ \mu_0 &= 4\pi\ 10^{-7}\ \text{H m}^{-1} \end{aligned}$$

Theoretical results give the scattered and diffracted magnetic fields as:

$$\begin{aligned} \mathbf{H}^s &= H_0 \sum_{n=-\infty}^{+\infty} a_n H_n^{(2)}(\beta_0\rho) e^{jn\phi}\mathbf{e}_z \\ \mathbf{H}^d &= H_0 \sum_{n=-\infty}^{+\infty} b_n J_n(\beta\rho) e^{jn\phi}\mathbf{e}_z \end{aligned} \tag{2}$$

where $\beta = \frac{\omega}{c}\sqrt{\varepsilon_r'}$ the propagation factor in DUT (lossless dielectric) and ε_r' the real dielectric constant (which is now replaced by "permittivity"), the coefficients a_n and b_n are developped in Eqs. (3) and (4) using boundary conditions verifying the continuity of electric and magnetic fields (tangential components). J_n and J_n' (resp. $H_n^{(2)}$ and $H_n'^{(2)}$) represent the Bessel (resp. Hankel) function of the first kind (resp. second kind) and its derivative.

$$a_n = j^{-n} \frac{J_n'(\beta_0 a) J_n(\beta a) - \sqrt{\mu_r/\varepsilon_r} J_n(\beta_0 a) J_n'(\beta a)}{\sqrt{\mu_r/\varepsilon_r} J_n'(\beta a) H_n^{(2)}(\beta_0 a) - J_n(\beta a) H_n'^{(2)}(\beta_0 a)} \tag{3}$$

$$b_n = j^{-n} \frac{J_n(\beta_0 a) H_n'^{(2)}(\beta_0 a) - J_n'(\beta_0 a) H_n^{(2)}(\beta_0 a)}{J_n(\beta a) H_n'^{(2)}(\beta_0 a) - \sqrt{\mu_r/\varepsilon_r} J_n'(\beta a) H_n^{(2)}(\beta_0 a)} \tag{4}$$

The scattered and reflected electrical field can be found from Maxwell's Ampere law:

$$\mathbf{E} = \frac{1}{j\omega\varepsilon}\nabla\times\mathbf{H} = \frac{1}{j\omega\varepsilon}\left(\frac{1}{\rho}\frac{\partial H_z}{\partial\phi}\mathbf{e}_\rho - \frac{\partial H_z}{\partial\rho}\mathbf{e}_\phi\right)$$

leading to:

$$\begin{aligned} \mathbf{E}^s &= \frac{H_0}{j\omega\varepsilon} \sum_{n=-\infty}^{+\infty} \left(\frac{jna_n}{\rho} H_n^{(2)}(\beta_0\rho)\mathbf{e}_\rho - \beta_0 a_n H_n'^{(2)}(\beta_0\rho)\mathbf{e}_\phi\right) e^{jn\phi} \\ \mathbf{E}^d &= \frac{H_0}{j\omega\varepsilon} \sum_{n=-\infty}^{+\infty} \left(\frac{jnb_n}{\rho} J_n(\beta\rho)\mathbf{e}_\rho - \beta b_n J_n'(\beta\rho)\mathbf{e}_\phi\right) e^{jn\phi} \end{aligned} \tag{5}$$

This solution can be calculated for a set of frequencies (in our work, 1601 frequencies in the range [1.5–15 GHz]). Then, the equivalent solution in the time domain can be deduced using the Inverse Fourier Transform (IFT). The $E_y(f)$ field is calculated using Eq. (6) for N frequencies. Finally, the field in the time domain, the so-called pulse, is obtained by simple IFT multiplied by the parameter S_{11} of the transmitting antenna used in our experiment.

$$E_y(t) = \frac{1}{N}\sum_{n=0}^{N-1} E_y(f) e^{-i2\pi\frac{f_n}{n}} S_{11}(f) \tag{6}$$

The basic processing applied to this signal leads to the calculation of the permittivity ε_r' of the DUT by a simple law based on the detection of the travel times between transmitter and receiver with and without the DUT:

$$\varepsilon_r' = ((t_t - \frac{D-d}{c})\frac{c}{d})^2 \tag{7}$$

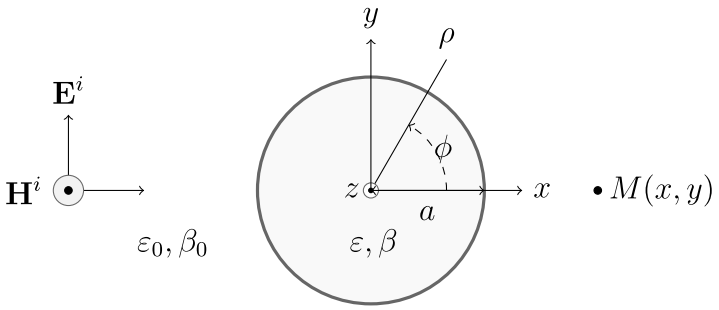

Fig. 1. TE^z polarization scattered by a circular cylinder of radius a, infinite in z-direction and with a permittivity of $\varepsilon = \varepsilon'_r \varepsilon_0$.

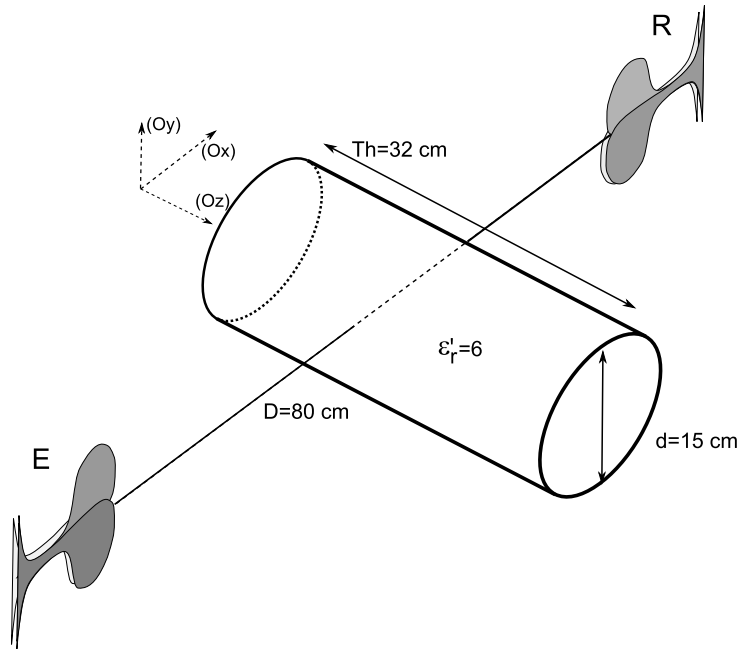

Fig. 2. First model to compare FDTD and analytical solution on a single layer cylindrical sample.

Where t_t represents the total propagation time in air and through the DUT, D the distance between port to port of the antennas and d the diameter of the sample (see Fig. 2). The travel time in the emitter and receiver is taken into account and its contribution disappears in the substraction of Eq. (7).

2.2. Finite difference in time domain simulation

2.2.1. First FDTD modelling compared with analytical approach: homogeneous cylinder composed of one dielectric material

In order to estimate the analytical approach, the system shown in Fig. 2 was modelled with FDTD (Finite-difference time domain) Empire XPU software (IMST GmbH). It consists of a homogeneous cylinder with permittivity $\varepsilon'_r = 6$, diameter $d = 15$ cm and thickness $Th = 32$ cm and two ETSA (7.2 cm * 7.2 cm * 0.9 cm) with a bandwith [1.5, 15 GHz], specifically adapted for this work. The model shows a measurement at one single position alongside the DUT, considered here as infinite thickness: the two antennas face each other, separated by a distance $D = 80$ cm, at a position z corresponding to the centre of the cylinder axis. The characteristics of these antennas are fully described in [49]. The frequency band was chosen so as to obtain, after IFT, a time-domain pulse with a half-height width of 0.22 ns. In most pavement materials considered to be lossless dielectrics, the true relative permittivity is between 4 and 9 [14]. In addition, the cores taken from pavements generally have a diameter of between 5 and 25 cm. The wavelength in the material is therefore between 2 and 3 cm, which is sufficient to characterize these samples in the time domain.

The result of the FDTD simulation shown in Fig. 3 is composed of six time pictures corresponding to:

- (a) At $t = 0.21$ ps, a pulse whose Fourier transform centred at 6 GHz (derivative of a Gaussian pulse), is generated at the input port of the transmitting antenna.
- (b) At $t = 1.02$ ns, the main pulse arrives at the DUT perimeter;
- (c) At $t = 1.69$ ns, according to Snell-Descartes law, a part of the energy is back-scattered to the transmitting antenna while (i) another part of the energy entered into the DUT and (ii) a diffracted (grazing) pulse turns around the DUT.
- (d) At $t = 2.31$ ns, the pulse arrives at the receiver antenna while the pulse inside the DUT is nearly to be diffracted at the frontier with the air.
- (e) At $t = 2.65$ ns, at the receiver port, the max energy of the pulse is recorded (see also Fig. 5) corresponding to the waves that travelled in air and turned around the DUT on a half-perimeter. Moreover, a diffracted pulse outside the DUT is forming.
- (f) At $t = 3.38$ ns, the pulse that passed through the DUT is recorded at the receiver port (see Fig. 5).

The field strength is recorded at the receiver port position and we plot the linear module of the pulse, with and without the DUT, for both analytical model and FDTD simulation. They are represented in Figs. 4 and 5, respectively.

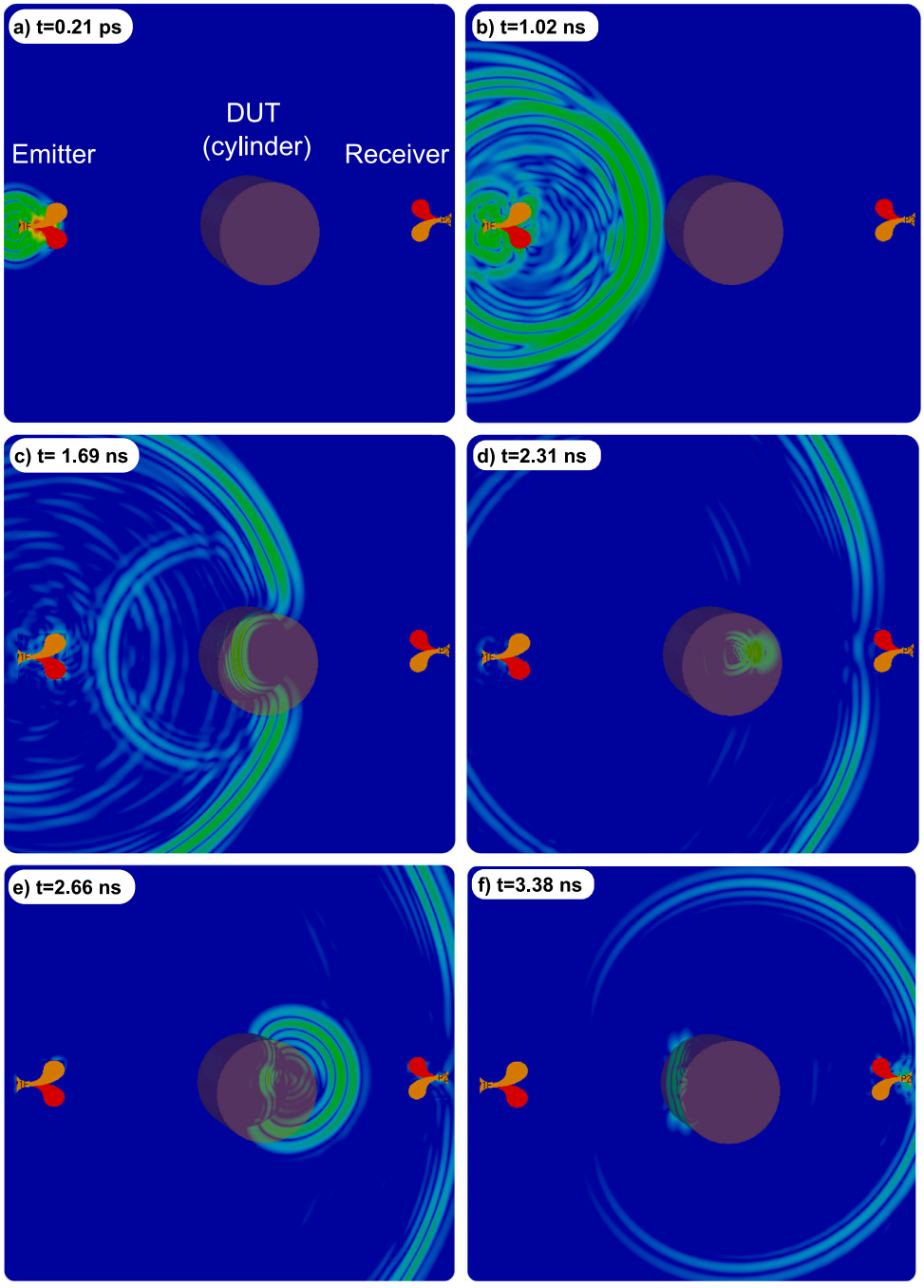

Fig. 3. Time evolution of pulse propagation within the electromagnetic bench. See explanation in the text for the six time steps from (a) to (e).

Without DUT, both time signals approximately present a maximum at the same location ($t_{air} = 2.66$ ns and $t_{air} = 2.67$ ns with analytical and FDTD solutions, respectively), representing the travel time of the pulse between the two antennas separated by a distance of D at the speed of c in air and at an unknown speed inside antennas. With DUT, three significant peaks are observed in FDTD simulation, and only one with analytical model: the first FDTD peak, located almost at the same time as the experiment without the DUT, corresponds to a grazing wave that circled the cylinder in the air. Regarding the absence of the first peak in the analytical solution, a more complete formulation would be to take into account the waves diffracted by grazing angles [50].

The second peak that is common in both analytical and FDTD solutions, at the time $t_t = 3.39$ ns and $t_t = 3.38$ ns respectively, corresponds to the pulse travelling through the DUT, the air and the antennas.

Table 1
Comparison of real permittivity results between analytical model and FDTD model (FDTD).

Solution	t_{air} (ns)	t_t (ns)	ε'_r	Relative error (%)
Analytical	2.66	3.39	5.98 ± 0.65	0.3
FDTD	2.67	3.38	5.88 ± 0.64	1

The third FDTD peak is a ripple of the second one, probably due to internal reflections within the simulated antenna. The relative error of the DUT permittivity between analytical and FDTD solutions with the permittivity of the model ($\varepsilon'_r = 6$) is 0.3% and 2%, respectively, which is acceptable for the characterization of a material. The uncertainty of the calculated permittivity is based on a time resolution $R = \frac{1}{Max_{Freq}}$

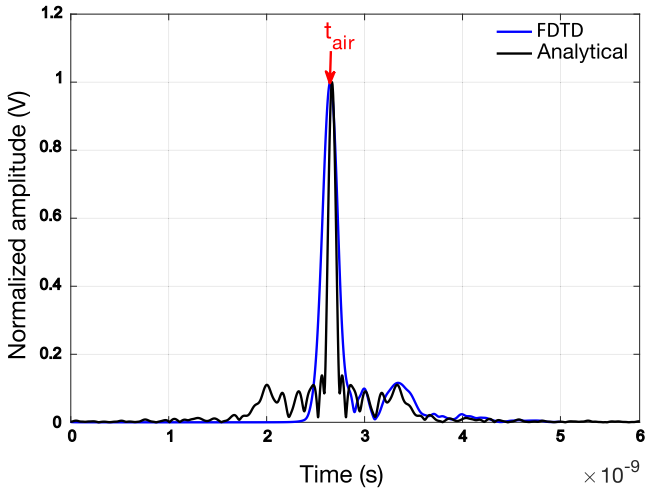

Fig. 4. Pulse (module) at the receiver after travel in the air (without DUT).

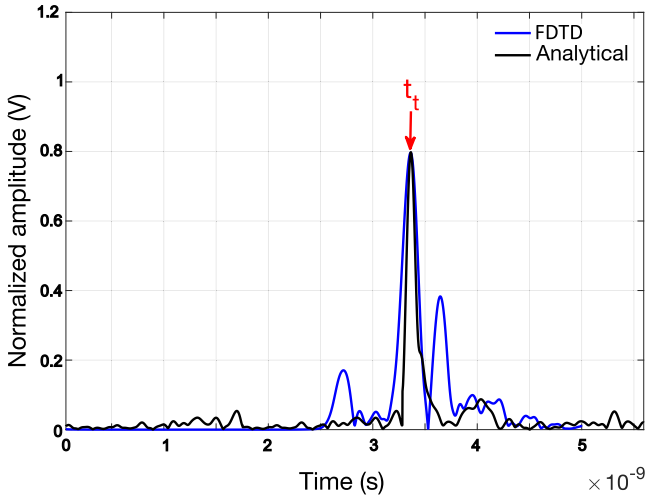

Fig. 5. Pulse (module) at the receiver after passing through the DUT. The first, second and third peaks correspond to a grazing wave circling the cylinder in the air, to the signal passing through the DUT recorded at t_t and to a ripple inside the DUT, respectively.

where Max_{Freq} = 15 GHz. In the present case, $R = 6.67.10^{-2}$ ns. All consequences of these values are discussed in the experimental section on HMA real cores for compaction assessment. All values of travel times and permittivities with and without the DUT are summarized in the Table 1.

2.2.2. Second FDTD modelling: core with several dielectric layers

In this second modelling shown in Fig. 6, we simulate in FDTD a full measurement alongside the multilayered DUT axis, as if we perform a tomography by moving both antennas in 0.5 cm steps in a direction parallel to the axis (Oz). The aim is also to highlight edge effects (diffraction of EM waves) at the cylinder bases/air transition or at the transition between two HMA layers. The two antennas are distant from D = 69.5 cm. The DUT with a diameter d = 15 cm and a thickness L = 32 cm, is composed of four layers of 5, 2, 10 and 15 cm thickness with a permittivity of $\varepsilon'_{r1} = 4$, $\varepsilon'_{r2} = 5$, $\varepsilon'_{r3} = 6$ and $\varepsilon'_{r4} = 7$, respectively. For each displacement, the pulse sent by the transmitting antenna E, is simulated. The amplitude of the field at the receiving antenna R for each position is recorded and reproduced as a B-scan as shown in Fig. 7. The abscissa axis is the scanning distance, i.e., the displacement of the antennas in (Oz) direction alongside the cylinder axis. The ordinate axis

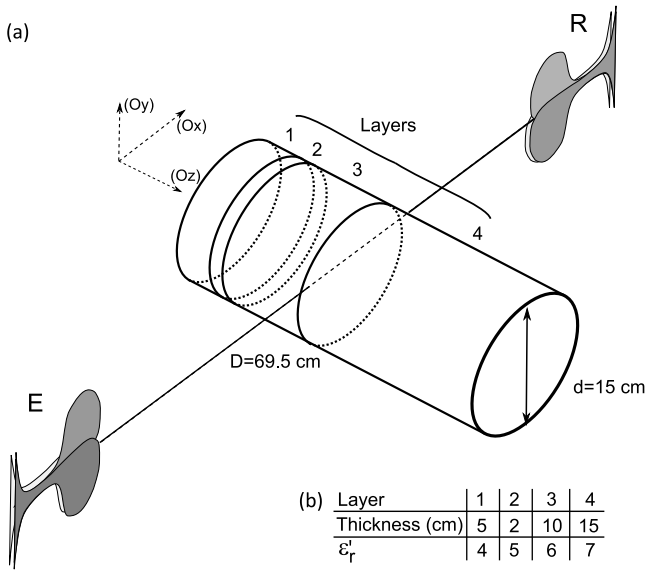

(b)

Layer	1	2	3	4
Thickness (cm)	5	2	10	15
ε'_r	4	5	6	7

Fig. 6. (a) Second model in FDTD to study edge effect of a multi-layer cylindrical sample. (b) The layer number, the thickness and the permittivity of the modelled DUT.

represents the propagation time of the pulse from the transmitter to the receiver and the grey-colour the nomalized amplitude of the pulse.

This B-scan presents three different zones: (1) the pulse corresponding to the propagation in the air (before and after encountering the DUT), (2) the pulse crossing the DUT, (3) the grazing pulse passing around the cylindrical sample.

The B-scan (Fig. 7, (a)) shows that the layers and the two bases of the DUT are delineated by hyperbola signatures, corresponding to diffraction between two media of different permittivity. In order to have a higher horizontal resolution, a classical processing signal in GPR domain is applied: the Kirchhoff migration (KM). KM is performed by using the Kirchhoff integral representation of a field at a given point as a superposition of waves propagating from adjacent points and times [51]. In two-dimensional (2D) case and in our coordinate system, (see Fig. 1 and let $x \rightarrow x + a$), we define $p(z, x = 0, t)$ the recorded data corresponding to the solution of the 2D-scalar Maxwell equation, where z, x, t are the surface coordinates along the scanning distance, the depth, and the time, respectively. The integral solution (8) is defined by Gazdag and Sguazzero [52] and Smitha et al. [53]:

$$p(z_1, x_1, t = 0) = \int \frac{\cos\theta}{\sqrt{2\pi r v}} \frac{\partial^{1/2} p}{\partial t}(z, x = 0, t = r/v) dz. \tag{8}$$

Where $v = \frac{1}{2}\frac{c}{\sqrt{\varepsilon_r}}$ is the half velocity, $r = \sqrt{(z_1 - z)^2 + x_1^2}$ is the radial distance from the source receiver location to the scatter-point and θ is the angle between the x-axis and the line passing through the (z_1, x_1) and $(z, x = 0)$ points. The factor $\sqrt{2\pi r v}$ takes into account for the 2D-spherical spreading. $\cos\theta$ compensates the diffraction amplitudes [54]. The result after migration is shown in Fig. 7, (b).

The objective is to estimate the DUT permittivity thanks to travel time picking on the module of the B-scans and using Eq. (7). We pick the travel time pulse of zone (1) in air and (2) after passing through the DUT of the Figs. 7, (a) and (b). This time is obtained by selecting, as in the first modelling, for each position of antennas along the DUT axis, the maximum of the module of the corresponding signal. The Fig. 8 shows the profile of the permittivity ε'_r of the sample as a function of the position of the antennas along the DUT axis. We note that the picking of travel times on the raw data (Fig. 7, (a)) induces errors (Fig. 8, blue crosses) in the assessment of the permittivity of the multilayer cylinder, since some of these picked times are positioned on the tails of the diffraction hyperbolas. Conversely, KM (Fig. 7, (b)) reduces the effects

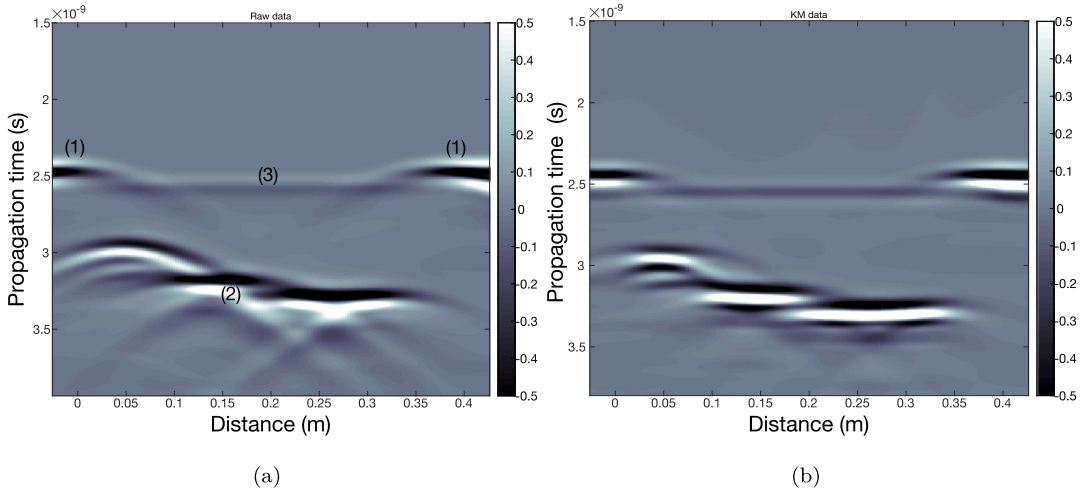

Fig. 7. FDTD B-scan of the second model (see Fig. 6): (a) raw data with (1) pulse in the air, (2) pulse passing through the 4-layer DUT and (3) grazing waves. (b) The same B-scan after KM processing.

(a)

Layer	1	2	3	4
Thickness (cm)	5	2	10	15
ε'_r	4	5	6	7

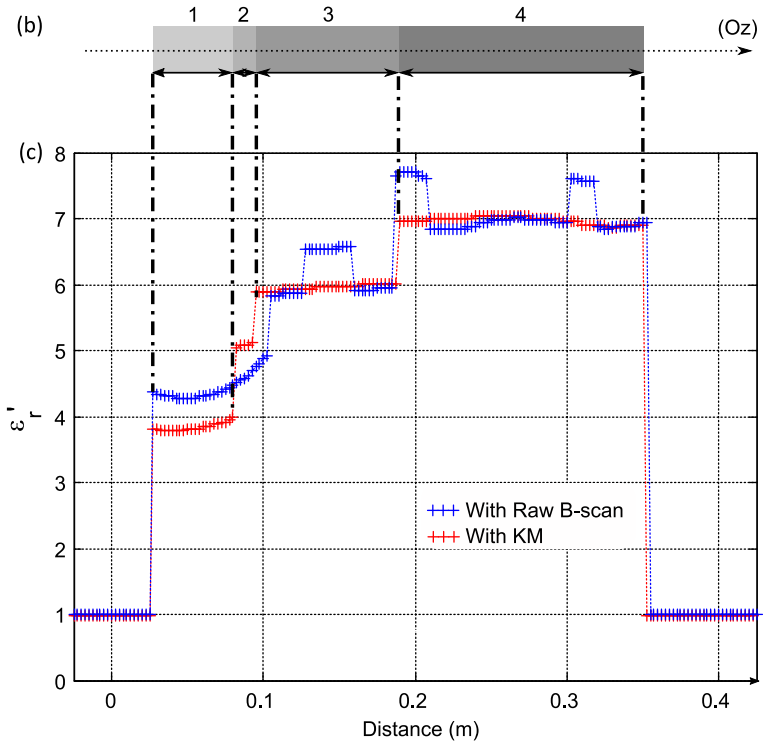

Fig. 8. The assessed permittivity using the FDTD results of the second multilayer system (see Fig. 6). (a) Main characteristics of the DUT layers. (b) Representation along (Oz) axis of the DUT with the layers' numbers. (c) With (red crosses) and without (blue crosses) KM, the assessed permittivity is obtained by travel time picking on the B-scans module of Fig. 7 and using Eq. (7). (For interpretation of the references to colour in this figure legend, the reader is referred to the web version of this article.)

of diffraction at layer transitions. It leads to more accurate picking and enables permittivities to be better evaluated, even for layers of the order of 2 cm thick (Fig. 8, red crosses). KM, first for seismic [52] and now for time-domain radar, represents a major advance in signal processing. In our case, it makes it possible to determine the permittivity (and therefore the compactness/density) of a multi-layer material, as is the case for samples taken from newly-paved roads.

2.2.3. Evaluation of the HMA density

Once the permittivity is assessed, EM mixing models are required to calculate the bulk density ρ_{HMAS} (also called bulk specific gravity) or compactness C of the HMA. The HMA is assumed to be a 4-phase material consisting of binder (b), filler (f), aggregates (a), and air (air). With EM bench, the permittivity of HMA is measured and is a function of the permittivity of each component, given by the following power

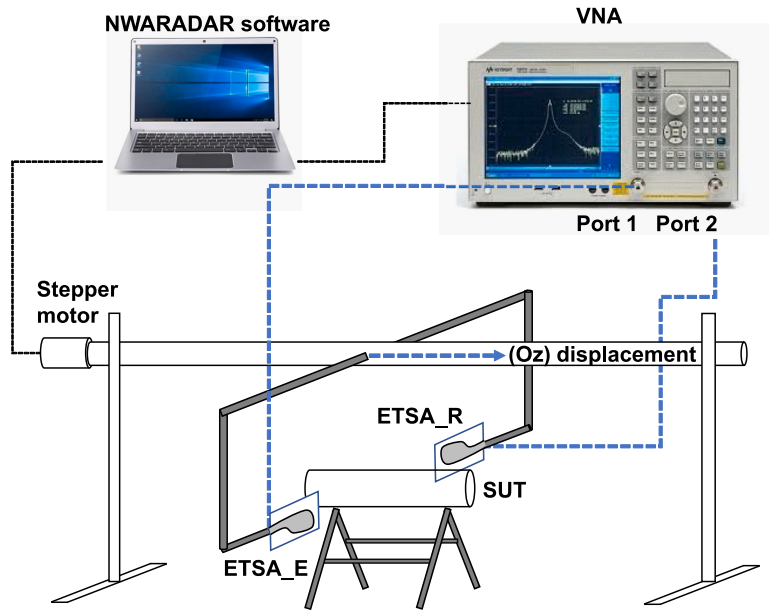

Fig. 9. EM bench components: The NWARADAR software drives the VNA that measures the S-parameter at a given position of the antennas. Once the measurement is achieved, the stepper motor moves to the next position and a new measurement is done.

law equation [11]:

$$(\varepsilon_r')^\alpha = \sum_i C_i(\varepsilon_i')^\alpha \tag{9}$$

With $i = [b, f, a, air]$. C_i is the volume concentration of the ith component. In this study, we choose $\alpha = \frac{1}{2}$ corresponding to the Complex Refractive Index Model (CRIM). The α parameter can have different values. Moreover, other models exist and have been tested. They can be found in the work of Araujo et al. [15]. Adapting Eq. (9) to the specific application of the 4-phase HMA compactness C evaluation gives the following equation [12]:

$$C = \frac{(\varepsilon_r')^\alpha - 1}{\frac{1}{Z}(\varepsilon_a')^\alpha + \frac{C_{rb}}{Z}(\varepsilon_b')^\alpha + \frac{C_{rf}}{Z}(\varepsilon_f')^\alpha - 1} \tag{10}$$

where C_{ri} is the relative volume concentration of the ith component and Z is equal to:

$$Z = 1 + \frac{\rho_a T_b}{\rho_b T_a} + \frac{\rho_a T_f}{\rho_f T_a} = 1 + C_{rb} + C_{rf} \tag{11}$$

Finally the density is simply related to the compactness by the following equation :

$$\rho_{HMAS} = C\rho_{HMAM} \tag{12}$$

where ρ_{HMAM} is the (maximum) specific gravity or the theoretical density for an air volume equal to 0.

For optimal accuracy in assessing compactness with the CRIM model, knowledge of the density ($\rho_{a,b,j}$), weight concentration ($T_{a,b,f}$) and permittivity ($\varepsilon'_{a,b,f}$) of each component is required. Road builders provide the HMA formulation, included all components density and weight concentrations as well as the specific gravity ρ_{HMAM}. The values of the permittivities of fillers (6) and binders (2.52) vary little from case to case across the world and, moreover, their proportion is low in the mixture. Therefore their contribution in the permittivity of the mix is low. Conversely, as the aggregates make up the main part of the mix, the knowledge of their permittivity is essential, especially since they vary in a significant range (from 4 to 9) depending on their geological origin [12,14]. Therefore and in most cases of study, the permittivity of aggregates is unknown and requires a specific dielectric characterization, conducted in cylindrical cavity for example [55]. Another solution is to obtain at least one core where the density is evaluated by standards (hydro-static weighing, nuclear methods) and where the aggregate permittivity is back-calculated. This last method is adopted in the experimental section and it is based on the use of a nuclear bench previously produced by the manufacturer.

3. Electromagnetic bench experiment in the laboratory for HMA denisty assessment

3.1. Description of the system

The EM bench shown in Figs. 9 and 10 consists of a VNA (Agilent E8362B) and two ETSA. The antennas are placed facing each other, separated by a distance D from port to port, the origin being fixed at the cable transition/antenna input. A DUT of diameter d is placed in the middle between antennas, which can move thanks to a stepper motor with a given step ranging from few mm to 1 cm along the (Oz) axis, corresponding to the cylinder axis.

The aim is the density/compactness assessment of HMA cylindrical samples. Materials are usually dried in oven in order to remove all potential water content. HMA are lossless dielectrics [12,13]. Consequently, only the real dielectric constant (called the permittivity) ε_r' of the sample is considered.

The entire EM bench is driven by a software [56] developed in the laboratory. At each step, a measurement of S_{21}-parameter is performed on 1601 frequencies ranging in [1.5–15] GHz, corresponding to the −10 dB threshold determined by measuring the S_{11}-parameters for each antenna. In order to have an optimal signal in the time domain thanks to the IFT, a zero-padding process out of the frequency band allows a better resolution and a Kaiser windowing [57] is applied on the S_{21}-parameter to smooth the contribution the second lobes [58].

3.2. Experimental results

3.2.1. Calibration

The EM bench was tested on various cylindrical samples in the laboratory. The first measurement was carried out on a cylindrical Teflon sample (see on the left of the Fig. 11) with a diameter $d = 8.5$ cm and a thickness $L = 32$ cm. Measurements were made for three different configurations as a function of the distance D between the two antennas

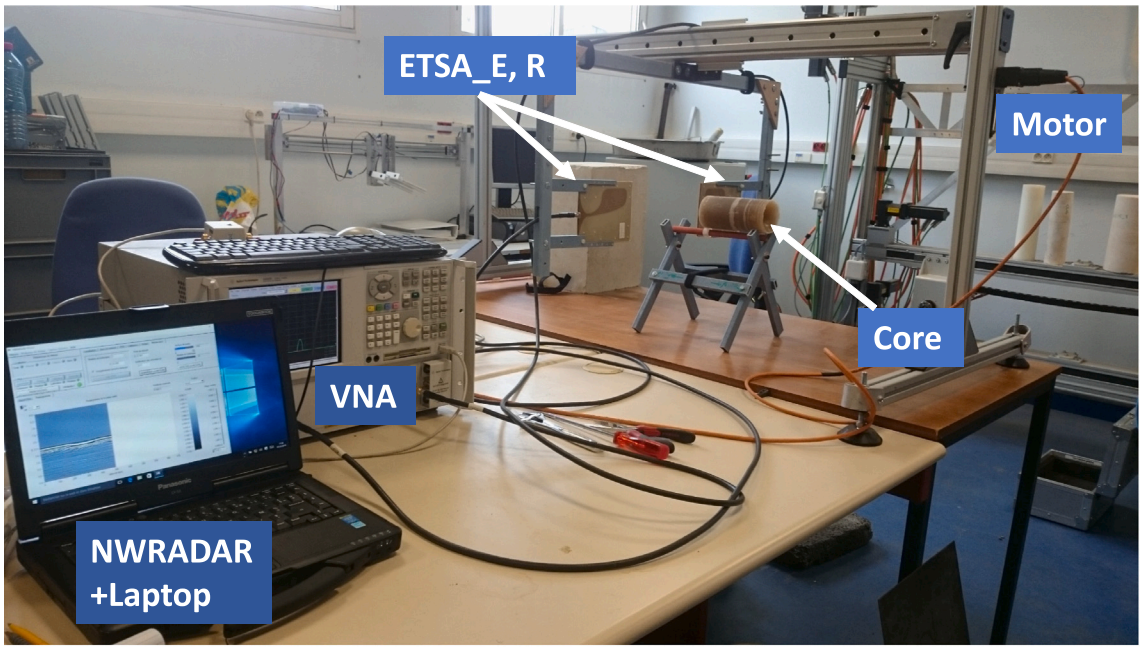

Fig. 10. EM bench in the laboratory during measurement.

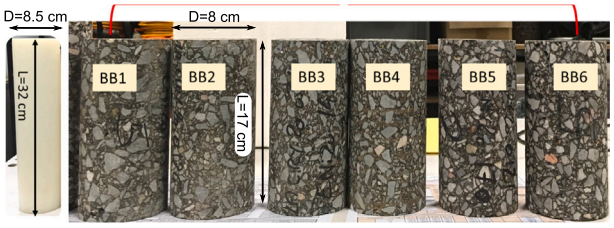

Fig. 11. Cylindrical samples of Teflon and HMA.

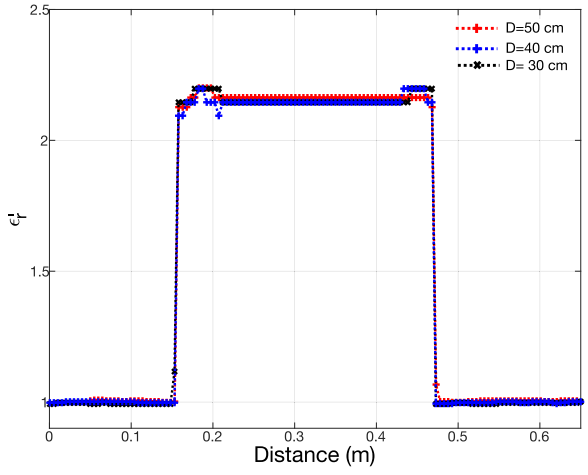

Fig. 12. Permittivity Profile of Teflon for D = 30, 40 and 50 cm.

(port to port); $D = 30$, 40 and 50 cm. The S_{21}-parameter is recorded in steps of 5 mm by 60 cm along the samples (see Table 2).

Under the assumption that Teflon is a non-dispersive material at the frequencies used, the comparisons between the mean permittivities obtained with the EM bench and with the cylindrical cavity reference method [14] are close to 0.2 to 0.6% for D=30 to 50 cm. These results also show that the distance between the two antennas has an influence

Table 2
Mean permittivity of a Teflon sample obtained with the EM bench for three emitter/receiver distances, compared with the mean permittivity measured in a cylindrical cavity at six frequencies (0.5, 1.1, 1.3, 2, 2.6, 4 GHz, see Araujo et al. [14]).

Distance (cm)	Mean of ϵ'_r measured	Reference of ϵ'_r	Relative error (%)
30	2.155 ± 0.02		0.23
40	2.149 ± 0.02	2.15 ± 0.1	0.25
50	2.165 ± 0.01		0.6

Table 3
HMA characteristics provided by the road builder.

Aggregates	BB1 & BB2 (0/10)	BB3 & BB4 (0/10)	BB5 & BB6 (0/10)
T_{ag}	0.957	0.954	0.947
T_b	0.033	0.026	0.043
T_f	0.01	0.02	0.01
ρ_{ag} (Mg/m^3)	2.8	2.8	2.543
ρ_b (Mg/m^3)	1.027	1.033	1.033
ρ_f (Mg/m^3)	2.8	2.8	2.8
ρ_{HMAM} (Mg/m^3)	2.548	2.591	2.461
ϵ'_f	6	6	6
ϵ'_b	2.52	2.52	2.52

on the results. As shown in Fig. 12, we notice for this first study that the closer to the sample the antennas are, the better the results.

3.2.2. Density/compactness assessment on HMA cores

The electromagnetic bench has been tested to assess the bulk density and the compactness of three pairs of HMA cores (BB1&BB2, BB3&BB4 and BB5&BB6, each pair having its own composition) with known formulations, of diameter $d = 8$ cm and length $L = 17$ cm. The distances between antennas is $D = 30$ cm. We use the same frequency band and data processing than the previous experiment. These samples are composed of aggregates (0/10), fines, bitumen and air. The mass content and density of each component as well as the real density (specific gravity) of the HMA are shown in the Table 3.

The only unknown is the permittivity of the aggregates. Unfortunately, we could not obtain a rock sample in order to control its permittivity in the cylindrical cavity, while according to Eq. (10), it is required to assess the compactness.

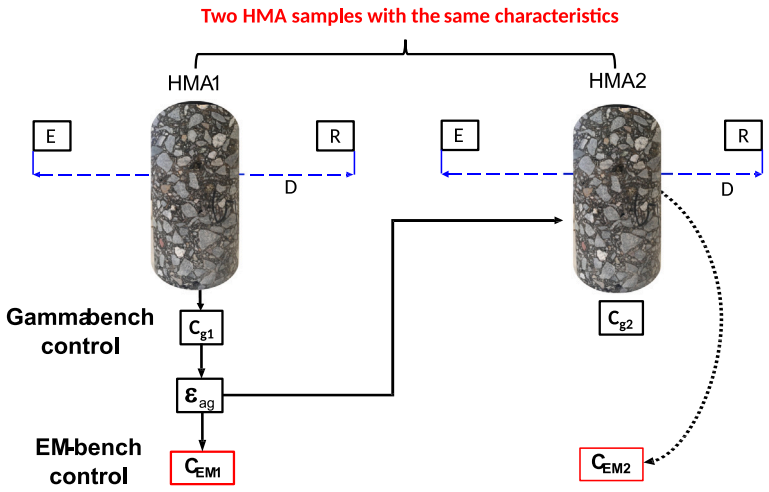

Fig. 13. The gamma bench control allows the HMA1 compactness to be assessed. The permittivity of HMA1 aggregates is calculated and its value is then inserted in Eq. (10) to assess the compactness of HMA2 with EM bench. Finally, the compactness of HMA2 is calculated based on HMA1 aggregates permittivity values.

Table 4
Comparison between the results obtained by the EM bench and by the gamma bench.

HMA	Gamma bench			EM bench			Relative error (%)
	ρ_a (Mg/m^3)	C_g	ε'_a	ε'_{bb}	ρ_a (Mg/m^3)	C_{EM}	
BB1	2.379 ± 0.017	0.933	**8.37**	7.04 ± 0,03	2.369 ± 0.009	0.929 ± 0.003	0.4
BB2	2.374 ± 0.02	0.931		7.02 ± 0.11	2.365 ± 0.03	0.928 ± 0.011	0.3
BB3	2.427 ± 0.02	0.936	**7.99**	6.86 ± 0.07	2.41 ± 0.02	0.932 ± 0.008	0.45
BB4	2.447 ± 0.025	0.944		6.84 ± 0.039	2.41 ± 0.011	0.931 ± 0.004	1.41
BB5	2.367 ± 0.02	0.95	**6.76**	5.81 ± 0.027	2.35 ± 0.009	0.944 ± 0.003	0.65
BB6	2.358 ± 0.016	0.946		5.81 ± 0.06	2.347 ± 0.022	0.942 ± 0.009	0.43

Firstly, the methodology starts with a calibration phase: the permittivity of the aggregates ε'_a of the first core BB1 is calculated from the compactness C_{g1} obtained by the nuclear gauge, previously performed by the road builder. Secondly, the compactness C_{EM1} is evaluated with the EM bench. Thirdly, the permittivity ε'_a is included in the calculation of the second core BB2, which has the same composition as BB1, to determine the compactness C_{EM2}. This procedure is repeated for pairs of samples BB3-BB4 and BB5-BB6. A schematic diagram is shown in Fig. 13.

The compactness of these cores was controlled in the laboratory with the nuclear gauge method according to the European standard [59]. For each sample, two measurements were made with the gamma bench to determine the bulk density. The mean of the two measurements is the reference. The B-scans of the six cores are shown in Fig. 14 and the compactness obtained with the EM bench along their axis (see Fig. 15) as well as the comparison with the results obtained by the gamma bench is shown in the Table 4:

The compactness values obtained from the permittivity measurements with the EM bench compared with those obtained by the gamma bench are very close and therefore acceptable in terms of accuracy (the majority of relative errors of less than 1%). This first experiment allows the general approach to be validated: assessing the compactness of the HMA based on the measurement of its permittivity and the knowledge of the characteristics of the constituents of the mix (permittivity, the mass content and the density).

4. Discussion

The measurement system presented had to meet two objectives: a low cost and simple approach. Firstly, it is based on a configuration with a receiver and a transmitter as well as a VNA. The latter is usually used in laboratories for very precise measurements of electronic components, and represents a high cost. We have tested our method with low-cost analysers and the results are equivalent. The UWB Vivaldi antennas represent a very reasonable cost and the technology used remains very affordable. Secondly, the assessment of density/compactness is based on the measurement of the real permittivity. Road samples are generally dried in oven before tests, their imaginary parts is low and they are considered as low-loss materials. Consequently, a simple approach based on the measure of the travel-time of waves in the time domain, as in GPR prospect ion, appears suitable to evaluate the permittivity of the cylinder. The density of the material can then be assessed using electromagnetic mixing laws.

For laboratory testing of the design of new pavements, the measured compactness must be within 1% of the true value. In our case, this would require knowing the true value of the permittivity of the HMA as well as that of the aggregate with an accuracy of less than 2%. This limit is respected in the laboratory on Teflon samples, as we have shown. It is more difficult to know whether the value measured with the electromagnetic bench is accurate or not on pavement samples. Nevertheless, these initial measurements show that the estimated compactness is of the same order as that obtained with the gamma bench. To achieve an accuracy of 2% on the permittivity values measured with the EM bench, the time resolution must be of the order of 1.33 ps. However, we are here limited in frequency to 15 GHz, and therefore to a resolution of 6.67 ps. To achieve the desired resolution, we increase the number of points in the Fourier domain by zero-padding a power-of-two number of samples. Of course, this technique does not remove the initial uncertainty of the measurement, but it does allow sufficiently accurate travel time measurements to achieve the desired resolution.

It is now necessary to continue the laboratory test measurements. Comparisons between the electromagnetic and nuclear approaches need to be based on more detailed statistical estimates, taking into account a wider range of sample characteristics (diameter, type of aggregate). Moreover, our experiment used the nuclear bench to calibrate the EM bench, as we seek to replace this method. Unfortunately, it was

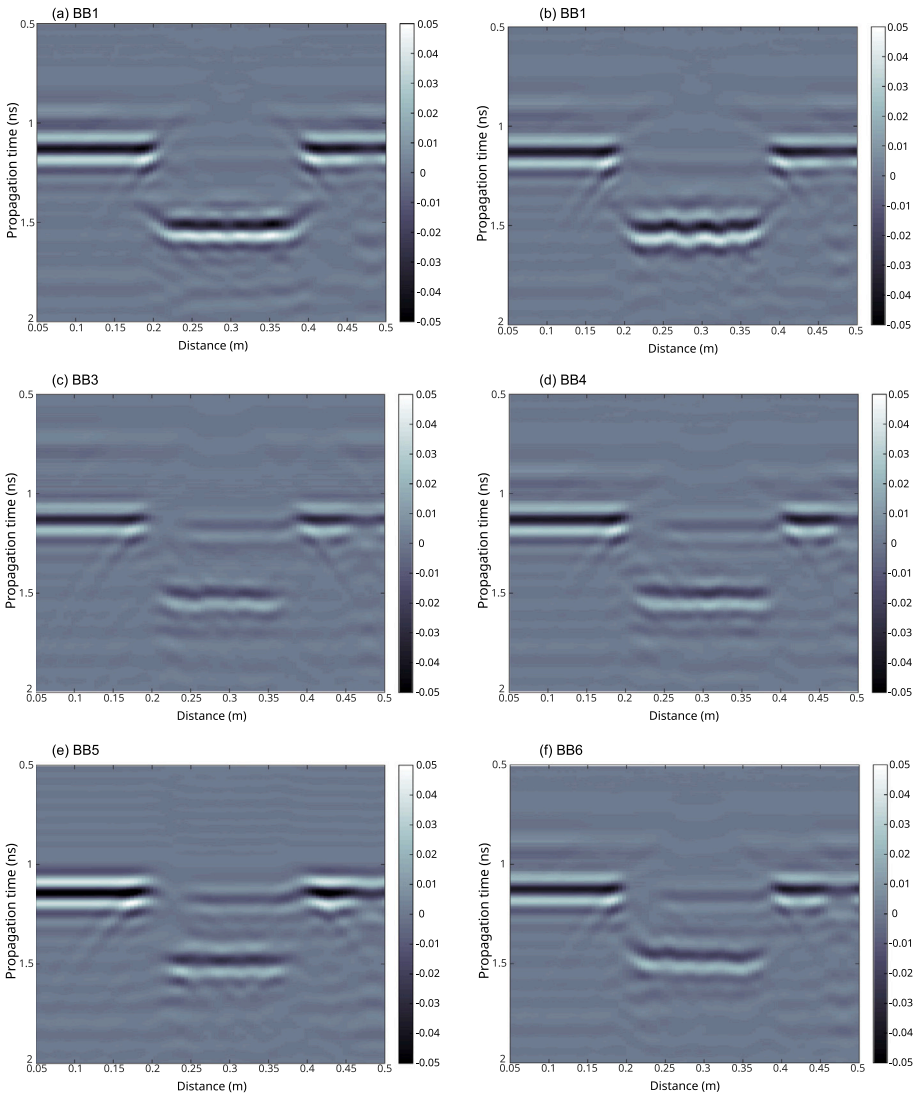

Fig. 14. B-scans measured with the data migrated for D = 30 cm for all HMA samples BB1 to BB6.

not possible to obtain aggregates samples to estimate their permittivity with cylindrical cavities.

While this initial approach validates the concept of an electromagnetic bench for the replacement of nuclear bench, many improvements could be envisaged. Increasing the number of transmitting and receiving antennas would certainly enable more complete results to be obtained, but this would be at the expense of the technical simplicity proposed. Rotating the sample would also give additional measurements along the cylinder axis. It could also take into account the geometric shape of the sample as a priori information in a direct model. The signal processing performed on these measurements is based on simple Kaiser-Beta filtering. This attenuates (i) low frequencies and the potential problems that can arise when making near-field measurements, and (ii) high frequencies which add parasitic ripples to the original signal, without compromising the time resolution needed to calculate travel times. However, our measurements are made in a laboratory environment where electromagnetic noise is present. Additional processing based on temporal windowing and consideration of antenna radiation patterns [60] would be worth investigating. Furthermore, it is not always possible to characterize antennas in anechoic chambers. Far-field correction techniques in a non-anechoic environment, based on the use of wavelets, would significantly improve the accuracy of delay measurements [61].

Finally, a more complete approach allowing an estimation of the permittivity in the frequency domain, over the whole range considered, should be envisaged for various types of samples. This would lead to study a wider range of materials, including those with non-negligible dielectric losses in Earth sciences (rocks, sands, clays) or in civil engineering (concrete, materials with green binder) and promising a wide range of applications.

5. Conclusion

The principle of electromagnetic tomography in time domain is used to replace the gamma bench (nuclear gauge in the laboratory) to assess the compactness and the density of road materials. We remind the theoretical basics of incident waves emitted by a point source, encountering a dielectric cylinder and the measure of the received waves after passing through and around the cylinder. Based on this configuration, a electromagnetic bench has been built. It is equipped with a vector network analyser and two Vivaldi antennas with a bandpass of [1.5–15 GHz]. It measures the wave travel time after passing through the cylinder and the permittivity of the sample is deduced. The measurement principle is validated on known samples (Teflon). Finally, six cylindrical cores of hot mix asphalt materials are tested and their compactness/density are assessed thanks to a electromagnetic mix law. Results are compared with the standard nuclear gauge in the

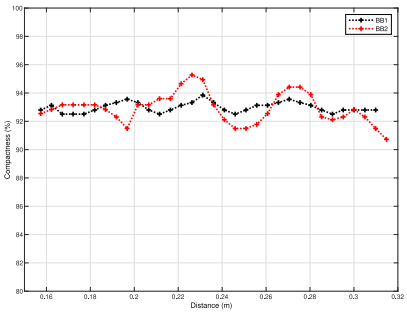

(a) BB2

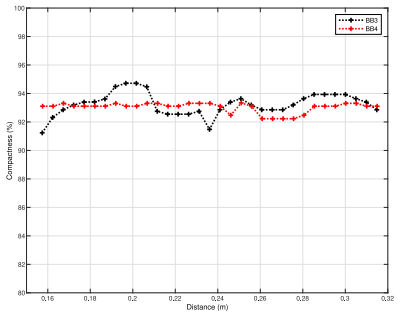

(b) BB4

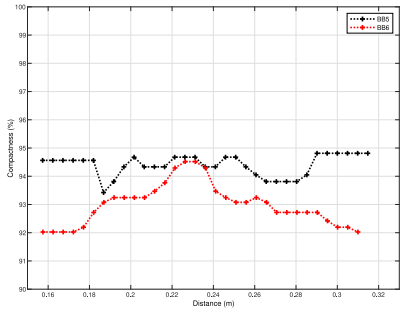

(c) BB6

Fig. 15. HMA compactness of the six cores.

laboratory. The EM bench gives satisfactory results and represents a very promising alternative to nuclear instrument for assessing density of materials.

CRediT authorship contribution statement

Cyrille Fauchard: Writing – review & editing, Visualization, Validation, Supervision, Resources, Methodology, Investigation, Formal analysis, Conceptualization. **Imen Boughanmi:** Writing – original draft, Visualization, Validation, Investigation. **Nabil Benjelloun:** Supervision, Conceptualization. **Riah Zouheir:** Supervision, Conceptualization. **Théau Cousin:** Writing – original draft, Software, Formal analysis. **Bruno Beaucamp:** Software, Resources. **Vincent Guilbert:** Visualization, Methodology.

Declaration of competing interest

The authors declare that they have no known competing financial interests or personal relationships that could have appeared to influence the work reported in this paper.

Data availability

Data will be made available on request.

Acknowledgement

The authors thank the Normandy Region who funded the project and Routes de France who continues to support our research.

References

[1] ASTM D6938 - 10. Standard Test Method for In Place Density and Water Content of Soil and Soil Aggregate by Nuclear Methods (Shallow Depth). Technical Report, ASTM International; 2010, http://dx.doi.org/10.1520/D6938-10, URL www.astm.org.

[2] ASTM D2950 / D2950M. Standard Test Method for Density of Bituminous Concrete in Place by Nuclear Methods. Technical Report, ASTM International; 2011, URL www.astm.org.

[3] NF P94-061-1. Sols : reconnaissance et essais - Détermination de la masse volumique d'un matériau en place - Partie 1 : méthode au gammadensimètre à pointe (à transmission directe). Technical Report, AFNOR; 1996.

[4] NF P94-062. Sols : reconnaissance et essais - Mesure de la masse volumique en place - Diagraphie à double sonde gamma. Technical Report, AFNOR; 1997.

[5] ASTM D7113 / D7113M. Standard Test Method for Density of Bituminous Paving Mixtures in Place by the Electromagnetic Surface Contact Methods. Technical Report, ASTM International; 2010, http://dx.doi.org/10.1520/D7113_D7113M-10, URL www.astm.org.

[6] Prowell BD, Dudley MC. Evaluation of measurement techniques for asphalt pavement density and permeability. Transp Res Rec 2002;1789(1):36–45. http://dx.doi.org/10.3141/1789-04, arXiv:https://doi.org/10.3141/1789-04.

[7] Hausman JJ, Buttlar WG. Analysis of TransTech model 300 pavement quality indicator: Laboratory and field studies for determining asphalt pavement density. Transp Res Rec 2002;1813(1):191–200.

[8] Ameri M, Novin MK, Yousefi B. Comparison of the field measurements of asphalt concrete densities obtained by ground-penetrating radar, pavement quality indicator and the borehole coring methods. Road Mater Pavement Des 2014;15(4):759–73. http://dx.doi.org/10.1080/14680629.2014.909874.

[9] Al-Qadi I, Leng Z, Lahouar S, Baek J. In-place hot-mix asphalt density estimation using ground-penetrating radar. Transp Res Record: J Transp Res Board 2010;2152(1):19–27. http://dx.doi.org/10.3141/2152-03.

[10] Leng Z, Al-Qadi IL, Lahouar S. Development and validation for in situ asphalt mixture density prediction models. NDT E Int 2011;44(4):369–75.

[11] Sihvola A. Mixing rules with complex dielectric coefficient. Subsurf Sens Technol Appl 2000;1:393–415.

[12] Fauchard C, Li B, Laguerre L, Héritier B, Benjelloun N, Kadi M. Determination of the compaction of hot mix asphalt using high-frequency electromagnetic methods. NDT E Int 2013;60:40–51. http://dx.doi.org/10.1016/j.ndteint.2013.07.004, URL https://www.sciencedirect.com/science/article/pii/S0963869513000972.

[13] Fauchard C, Beaucamp B, Laguerre L. Non-destructive assessment of hot mix asphalt compaction/ density with a step-frequency radar: case study on a newly

paved road. Near Surface Geophys 2015;13(3):pp.289–297. http://dx.doi.org/10.3997/1873-0604.2015009.
[14] Araujo S, Delbreilh L, Laguerre L, Dumont H, Dargent E, Fauchard C. Rock permittivity characterization and application of electromagnetic mixing models for density/compactness assessment of HMA by means of step-frequency radar. Near Surface Geophys 2016;14(6):551–62. http://dx.doi.org/10.3997/1873-0604.2016031.
[15] Araujo S, Beaucamp B, Delbreilh L, Dargent E, Fauchard C. Parametric study of the compactness assessment of a new road containing recycled asphalt pavement through non-nuclear method. In: 2017 9th international workshop on advanced ground penetrating radar. IWAGPR, 2017, p. 1–5. http://dx.doi.org/10.1109/IWAGPR40444.2017.
[16] Baron J, Peyernard J. Mesure de la densité par diffusion gamma à l'aide d'un appareil expérimental.. Bull Liaison Lab Routiers 1968;34:47–64.
[17] Abbosh AM, Kan HK, Bialkowski ME. Compact ultra-wideband planar tapered slot antenna for use in a microwave imaging system. Microw Opt Technol Lett 2006;48(11):2212–6. http://dx.doi.org/10.1002/mop.21906.
[18] Jalilvand M, Vasanelli C, Wu C, Kowalewski J, Zwick T. On the evaluation of a proposed bowtie antenna for microwave tomography. In: The 8th European conference on antennas and propagation. euCAP 2014, 2014, p. 2790–4.
[19] Li X, Davis SK, Hagness SC, van der Weide DW, Van Veen BD. Microwave imaging via space-time beamforming: experimental investigation of tumor detection in multilayer breast phantoms. IEEE Trans Microw Theory Tech 2004;52(8):1856–65.
[20] Abbosh A, Mohammed B, Bialkowski M. Planar array antenna for ultra wideband microwave imaging system. In: 2011 international conference on communications and information technology. ICCIT, 2011, p. 199–202. http://dx.doi.org/10.1109/ICCITECHNOL.2011.5762679.
[21] Stang JP, Joines WT. Tapered microstrip patch antenna array for microwave breast imaging. In: 2008 IEEE MTT-s international microwave symposium digest. 2008, p. 1313–6.
[22] Meaney PM, Fanning MW, di Florio-Alexander RM, Kaufman PA, Geimer SD, Zhou T, Paulsen KD. Microwave tomography in the context of complex breast cancer imaging. In: 2010 annual international conference of the IEEE engineering in medicine and biology. 2010, p. 3398–401.
[23] Gilmore C, Mojabi P, Zakaria A, Ostadrahimi M, Kaye C, Noghanian S, Shafai L, Pistorius S, LoVetri J. An ultra-wideband microwave tomography system: Preliminary results. In: 2009 annual international conference of the IEEE engineering in medicine and biology society. 2009, p. 2288–91.
[24] Ahsan S, Guo Z, Miao Z, Sotiriou I, Koutsoupidou M, Kallos E, Palikaras G, Kosmas P. Design and Experimental Validation of a Multiple-Frequency Microwave Tomography System Employing the DBIM-TwIST Algorithm. Sensors (Basel, Switzerland) 2018;18(10:3491). http://dx.doi.org/10.3390/s18103491.
[25] Gilmore C, Mojabi P, Zakaria A, Ostadrahimi M, Kaye C, Noghanian S, Shafai L, Pistorius S, LoVetri J. A wideband microwave tomography system with a novel frequency selection procedure. IEEE Trans Biomed Eng 2010;57(4):894–904.
[26] Amineh RK, Ravan M, Trehan A, Nikolova NK. Near-field microwave imaging based on aperture raster scanning with TEM horn antennas. IEEE Trans Antennas and Propagation 2011;59:928–40. http://dx.doi.org/10.1109/TAP.2010.2103009.
[27] Yu C, Yuan M, Stang J, Bresslour E, George RT, Ybarra GA, Joines WT, Liu QH. Active microwave imaging II: 3-D system prototype and image reconstruction from experimental data. IEEE Trans Microw Theory Tech 2008;56(4):991–1000.
[28] Yu C, Yuan M, Zhang Y, Stang J, George RT, Ybarra GA, Joines WT, Liu QH. Microwave imaging in layered media: 3-D image reconstruction from experimental data. IEEE Trans Antennas and Propagation 2010;58(2):440–8.
[29] Jean-Michel G, Sabouroux P, Eyraud C. Free space experimental scattering database continuation: Experimental set-up and measurement precision. Inverse Problems 2005;21:S117.
[30] Eyraud C, Geffrin J, Litman A. 3D-aggregate quantitative imaging: Experimental results and polarization effects. IEEE Trans Antennas and Propagation 2011;59(4):1237–44.
[31] K Amineh R, Khalatpour A, Xu H, Baskharoun Y, Nikolova N. Three-dimensional near-field microwave holography for tissue imaging. Int J Biomed Imaging 2012;2012:291494.
[32] Rubaek T, Kim OS, Meincke P. Computational validation of a 3-D microwave imaging system for breast-cancer screening. IEEE Trans Antennas and Propagation 2009;57(7):2105–15.
[33] Zhurbenko V, Rubaek T, Krozer V, Meincke P. Design and realisation of a microwave three-dimensional imaging system with application to breast-cancer detection. IET Microw Antennas Propag 2010;4(12):2200–11.
[34] Jensen PD, Rubaek T, Mohr JJ, Zhurbenko V. Nonlinear 3-D microwave imaging for breast-cancer screening: Log, phase and log-phase formulation. In: 2011 loughborough antennas propagation conference. 2011, p. 1–4.
[35] Jensen PD, Rubaek T, Mohr JJ. Utilization of multiple frequencies in 3D nonlinear microwave imaging. In: 2012 6th European conference on antennas and propagation. EUCAP, 2012, p. 1776–9.
[36] Haynes M, Stang J, Moghaddam M. Microwave breast imaging system prototype with integrated numerical characterization. Int J Biomed Imaging 2012;2012:706365.
[37] Stang J, Haynes M, Carson P, Moghaddam M. A preclinical system prototype for focused microwave thermal therapy of the breast. IEEE Trans Bio-Med Eng 2012;59:2431–8.
[38] Gilmore C, Mojabi P, Zakaria A, Pistorius S, LoVetri J. On super-resolution with an experimental microwave tomography system. IEEE Antennas Wirel Propag Lett 2010;9:393–6.
[39] Gilmore C, Zakaria A, Mojabi P, Ostadrahimi M, Pistorius S, Lo Vetri J. The university of manitoba microwave imaging repository: A two-dimensional microwave scattering database for testing inversion and calibration algorithms [measurements corner]. IEEE Antennas Propag Mag 2011;53(5):126–33.
[40] Yang F, Mohan AS. Microwave imaging for breast cancer detection using vivaldi antenna array. In: 2012 international symposium on antennas and propagation. ISAP, 2012, p. 479–82.
[41] Ahsan S, Kosmas P, Sotiriou I, Palikaras G, Kallos E. Balanced antipodal vivaldi antenna array for microwave tomography. In: 2014 IEEE conference on antenna measurements applications. CAMA, 2014, p. 1–3. http://dx.doi.org/10.1109/MOBIHEALTH.2014.7015974.
[42] Fang Q, Meaney PM, Paulsen KD. Microwave image reconstruction of tissue property dispersion characteristics utilizing multiple-frequency information. IEEE Trans Microw Theory Tech 2004;52(8):1866–75.
[43] Winters D, Shea J, Kosmas P, Van Veen B, Hagness S. Three-dimensional microwave breast imaging: Dispersive dielectric properties estimation using patient-specific basis functions. Med Imaging IEEE Trans 2009;28:969–81.
[44] Takenaka T, Jia H, Tanaka T. Microwave imaging of electrical property distributions by a forward-backward time-stepping method. J Electromagn Waves Appl 2000;14(12):1609–26.
[45] Fhager A, Gustafsson M, Nordebo S. Image reconstruction in microwave tomography using a dielectric debye model. IEEE Trans Bio-Med Eng 2011;59:156–66.
[46] Shahzad A, O'Halloran M, Jones E, Glavin M. A multistage selective weighting method for improved microwave breast tomography. Comput Med Imaging Graph 2016;54.
[47] Pellinen T, Huuskonen-Snicker E, Eskelinen P, Olmos Martinez P. Representative volume element of asphalt pavement for electromagnetic measurements. J Traffic Transp Eng (Engl Ed) 2015;2(1):30–9. http://dx.doi.org/10.1016/j.jtte.2015.01.003, URL https://www.sciencedirect.com/science/article/pii/S2095756415000045. Special Issue: Functional Pavement Materials and Characterization.
[48] Balanis CA. Advanced Engineering Electromagnetics. New York: Wiley; 1989.
[49] Boughanmi I. Contribution au développement, à la validation et à l'expérimentation d'un banc de caractérisation diélectrique des matériaux en tomographie électromagnétique (Ph.D. thesis), Normandie Université; 2021, URL https://theses.hal.science/tel-03325279.
[50] Wait JR, Conda AM. Diffraction of electromagnetic waves by smooth obstacles for grazing angles. J Res Natl Bureau Stand Sect D: Radio Propag 1959;181, URL https://api.semanticscholar.org/CorpusID:56210820.
[51] Liu X, Serhir M, Kameni A, Lambert M, Pichon L. Ground penetrating radar data imaging via Kirchhoff migration method. In: 2017 international applied computational electromagnetics society symposium - Italy. ACES, 2017, p. 1–2. http://dx.doi.org/10.23919/ROPACES.2017.7916395.
[52] Gazdag J, Sguazzero P. Migration of seismic data. Proc IEEE 1984;72(10):1302–15.
[53] Smitha N, Ullas Bharadwaj DR, Abilash S, Sridhara SN, Singh V. Kirchhoff and F-K migration to focus ground penetrating radar images. Int J Geo-Eng 2016;7(1):4. http://dx.doi.org/10.1186/s40703-016-0019-6.
[54] Özdemir C, Demirci Ş, Yiğit E, Yilmaz B. A review on migration methods in B-scan ground penetrating radar imaging. Math Probl Eng 2014;2014:280738. http://dx.doi.org/10.1155/2014/280738.
[55] Araujo S, Beaucamp B, Delbreilh L, Dargent, Fauchard C. Compactness/density assessment of newly-paved highway containing recycled asphalt pavement by means of non-nuclear method. Constr Build Mater 2017;154:1151–63. http://dx.doi.org/10.1016/j.conbuildmat.2017.07.075.
[56] Beaucamp B. NWARADAR 3.2.2, Manuel utilisateur version 1.0.0. In: CETE Normandie Centre. Technical Report, Cerema; 2013, doi:hal-04233788v1.
[57] Kaiser J, Schafer R. On the use of the I0-sinh window for spectrum analysis. IEEE Trans Acoust Speech Signal Process 1980;28(1):105–7.
[58] Seyfried D, Schoebel J. Stepped-frequency radar signal processing. J Appl Geophys 2015;112:42–51. http://dx.doi.org/10.1016/j.jappgeo.2014.11.003, URL https://www.sciencedirect.com/science/article/pii/S092698511400322X.
[59] NF P98-250-5. Essais relatifs aux chaussées Préparation des mélanges hydrocarbonés Partie 5 : Mesure en laboratoire de la masse volumique apparente d'un corps d'épreuve au banc Gammadensimétrique. Technical Report, 1993.
[60] Bekasiewicz A, Koziel S, Czyz M. Time-gating method with automatic calibration for accurate measurements of electrically small antenna radiation patterns in Non-Anechoic environments. Measurement 2023;208:112477. http://dx.doi.org/10.1016/j.measurement.2023.112477, URL https://www.sciencedirect.com/science/article/pii/S0263224123000416.
[61] Bekasiewicz A, Waladi V. Automatic correction of Non-Anechoic antenna measurements using complex morlet wavelets. IEEE Antennas Wirel Propag Lett 2024;1–5. http://dx.doi.org/10.1109/LAWP.2024.3398656.